

# Modulated Phases: Review and Recent Results<sup>†</sup>

David Andelman\*

Raymond and Beverly Sackler School of Physics and Astronomy, Tel Aviv University, Ramat Aviv, Tel Aviv 69978, Israel

Ronald E. Rosensweig<sup>‡</sup>

34 Gloucester Road, Summit, New Jersey 07901

Received: September 1, 2008; Revised Manuscript Received: September 20, 2008

We consider aspects of patternings that occur in a wide array of physical systems due to interacting combinations of dipolar, interfacial, charge exchange, entropic, and geometric influences. We review well-established phenomena as a basis for discussion of more recent developments. The materials of interest range from bulk inorganic solids and polymer organic melts to fluid colloids. Often, there are unifying principles behind the various modulated structures, such as the competition between surface or line tension and dipolar interaction in thermally reversible systems. Generally, their properties can be understood by free-energy minimization.

## I. Introduction

A diverse number of physical, chemical, and biological systems exhibit some type of modulation in their structural properties.<sup>1</sup> Examples of such structures in two-dimensional (2D) systems are elongated stripes and compact droplet-like domains, as can be seen in Figure 1. In the figure, domains in solid magnetic systems (garnet films) and in thin layers of ferrofluids (to be discussed in detail below) are shown side-by-side and exhibit striking similarity. In three-dimensional (3D) systems, the domain morphology can be more complex and includes sheets, tubes, rods, and droplets embedded in a three-dimensional matrix. The similarity between the resulting patterns in certain systems of different origins is quite surprising and may allude to a common unifying mechanism. In other cases additional mechanisms arise, as will be discussed.

It is convenient to view these systems as systems which, due to a competition between different interactions, achieve thermodynamic equilibrium in a state in which the appropriate order parameter shows a spatial modulation. Examples are abundant<sup>1</sup> and include modulation of the magnetization field of ferromagnetic slabs<sup>6–8</sup> and ferrofluids,<sup>3</sup> the polarization field in electric dipolar systems and certain liquid crystalline phases,<sup>9,10</sup> the superconducting order parameter in the intermediate phase of type I superconductors,<sup>11</sup> as well as the relative composition in block copolymer systems.<sup>12–14</sup>

We present in this paper some of the interesting phenomena associated with modulated phases. We start by considering a simple example explaining the underlying mechanism of wavelength selection in a quasi two-dimensional dipolar system. We then address domains in magnetic garnet films and related dipolar organic films at the water/air interface (Langmuir monolayers). Two other examples of systems of current scientific interest having many applications are subsequently discussed, mesophases in block copolymers and magnetic fluids (ferrofluids). Competing interactions create interesting new

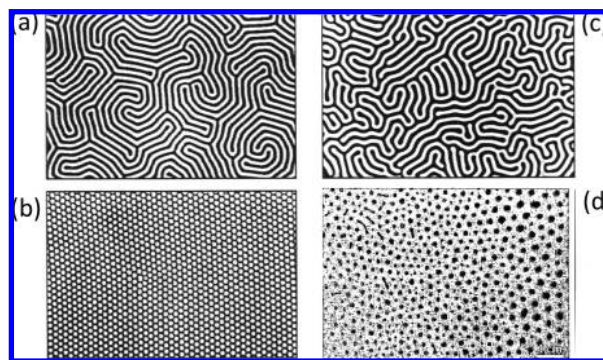


**Figure 1.** Domains in magnetic solids and fluids. (a) Stripes and (b) bubble phase in a ferromagnetic garnet film of 13 μm thickness grown on the (111) face of gadolinium gallium garnet. Visualization is made using polarized optical microscopy (Faraday effect). Period:  $d^* \sim 10 \mu\text{m}$ . Adapted from ref 2. (c) Ferrofluid confined between two glass plates exhibiting labyrinthine instability in a magnetic field.<sup>3,4</sup> The period is  $d^* \sim 2 \text{ mm}$ . (d) Bubble phase of a ferrofluid confined in a cell having a gap that increases from left to right. The mean bubble size is  $\sim 1 \text{ mm}$ . Adapted from ref 5.

phenomena when these systems are subjected to an external field (electric, magnetic), and we describe their morphology, structure, phase separation, various instabilities, and related phenomena.

## II. Domains in Two-Dimensional Ferromagnetic Layers

Ferromagnetism is an important physical phenomenon associated with elements like nickel, iron, and cobalt, as well as a large number of metallic alloys that show spontaneous magnetization  $M$  in the absence of an external applied magnetic field.

In bulk magnetic systems, the uniform magnetization does not persist throughout the system but breaks up into spatial domains, each having a specific and distinct magnetic orientation. The domain size and its structure depend on competing interactions inside of the magnet: the direct exchange interaction, the demagnetization fields, and the crystal anisotropy.

<sup>†</sup> Part of the "PGG (Pierre-Gilles de Gennes) Memorial Issue".

\* Corresponding author. E-mail: andelman@post.tau.ac.il.

<sup>‡</sup> E-mail: rosen1@verizon.net.

In order to explain on general grounds why dipolar systems prefer to break into domains of a well-defined size, we use the following simplified model for two-dimensional layers, which gives the essential features without the need to review all of the technical details. This model is applied in later sections to explains analogous features of magnetic garnet and films and dipolar Langmuir layers and is related to the labyrinthine instability of ferrofluids, as will be discussed below.

We consider a monomolecular layer of atomic dipoles in the  $(x, y)$  plane, each having a magnetic dipole (electronic spin) that can point only along the perpendicular  $z$  direction. The spins are taken to possess two possible values,  $S^z = \pm(1/2)$ , related to the two values of the atomic magnetic moment  $m = g_0 \mu_B S^z$ , where  $g_0 \mu_B$  is the gyromagnetic factor,  $\mu_B = e\hbar/2m_e c$  is the Bohr magneton, and  $g_0 \approx 2$  is the  $g$  factor. The system can be described using an Ising model with nearest-neighbor-only ferromagnetic coupling and the direct exchange interaction between adjacent spins minimized when two neighboring spins point in the same direction. Therefore, at low enough temperatures, the magnetic order will be (Ising-like) ferromagnetic.

By treating the Ising monolayer defined above at a coarse-grained level, we can perform the thermal average, namely, to sum with the proper Boltzmann weight factor over the microscopic spin degrees of freedom at finite temperatures. A local magnetization field for this 2D system,  $\mathcal{M}(\mathbf{r})$ , can be defined as a continuous function of the 2D position  $\mathbf{r}$ . Close to the Curie temperature  $T_c$  and at zero applied magnetic field  $H$ , the magnetization is small, and the ferromagnetic ( $\mathcal{M} \neq 0$ ) to paramagnetic ( $\mathcal{M} = 0$ ) transition can be described by an expansion of the free energy expressed in powers of  $\mathcal{M}$  and its gradient. This is the starting point of the well-known Ginzburg–Landau theory.<sup>15</sup> Because of the up–down spin symmetry in the absence of an orienting field, an expansion of the free energy has only even powers in  $\mathcal{M}$ , and up to fourth order in  $\mathcal{M}$ , it can be written as

$$\mathcal{F}_{\text{GL}} = \int d^2\mathbf{r} \left[ \frac{c}{2} |\nabla \mathcal{M}|^2 + \frac{\alpha}{2} \mathcal{M}^2(\mathbf{r}) + \frac{\beta}{4} \mathcal{M}^4(\mathbf{r}) \right] \quad (1)$$

The parameter  $c > 0$  (related to the direct exchange interaction),  $\alpha \sim T - T_c$ , and  $\beta > 0$  are phenomenological parameters. The uniform state of the system, in which the magnetization is independent of position, can be obtained from the above free energy expression by minimizing the integrand without the gradient term. For  $T < T_c$ ,  $\alpha < 0$  and the minimization yields two possible ferromagnetic states,  $\mathcal{M}(T) = \pm \mathcal{M}_0 = \pm(|\alpha|/\beta)^{1/2}$ , while for  $T > T_c$ , the only solution is the paramagnetic state,  $\mathcal{M} = 0$ .

Any two magnetic spins  $(i, j)$  also have a dipolar interaction leading to demagnetization terms which need to be included in the free energy. We consider the addition of these long-range interactions for Ising spins because these interactions have an important effect on the magnetic domain size. Any two colinear Ising spins,  $S_i^z$  and  $S_j^z$ ,  $S_i^z = \pm(1/2)$ , located in the  $(x, y)$  plane, distance  $r$  apart and pointing in the  $z$  direction have a dipolar interaction  $U_{ij}$

$$U_{ij} = \frac{m_i m_j}{4\pi\mu_0 r^3} = \frac{(g_0 \mu_B)^2 S_i^z S_j^z}{4\pi\mu_0 r^3} \quad (2)$$

where  $m_i = g_0 \mu_B S_i^z$  is the magnetic moment of the  $i$ th atom and  $\mu_0$  the vacuum permeability.

The coarse-grained dipolar magnetic energy can be derived from eq 2 and after thermal averaging is written as

$$\mathcal{F}_d = \frac{\mu_0}{8\pi} \int d^2\mathbf{r} d^2\mathbf{r}' \mathcal{M}(\mathbf{r}) g(\mathbf{r}, \mathbf{r}') \mathcal{M}(\mathbf{r}') \quad (3)$$

where the double integral is taken over all possible dipole pairs. The  $(1/2)$  prefactor is included in order to avoid double counting of pairs. The kernel  $g(\mathbf{r}, \mathbf{r}') = 1/|\mathbf{r} - \mathbf{r}'|^3$  expresses the long-range nature of the dipole–dipole interaction, eq 2. The integral in eq 3 can subsequently be manipulated more conveniently in Fourier space. Using  $\mathcal{M}_q$  and  $G(q)$  as the 2D Fourier transform of  $\mathcal{M}(\mathbf{r})$  and  $g(r)$ , respectively, we obtain

$$\begin{aligned} \mathcal{F}_d &= \frac{\mu_0}{32\pi^3} \int d^2\mathbf{q} \mathcal{M}_q G(q) \mathcal{M}_{-q} \\ &\approx -\frac{\mu_0}{32\pi^3} g_1 \int d^2\mathbf{q} |q| \mathcal{M}_q \mathcal{M}_{-q} \end{aligned} \quad (4)$$

Because  $g(r) = 1/r^3$ , where  $r = |\mathbf{r}|$  is the vectorial magnitude, the small  $q$  behavior of its Fourier transform  $G(q) = \int d^2\mathbf{r} g(r) \exp(-i\mathbf{q} \cdot \mathbf{r})$  is  $G(q) \approx -g_1 |q|$ , and a lower length cutoff,  $r = a$ , has to be introduced in the integration of eq 4 in order to take care of the diverging of  $g(r) = 1/r^3$  at  $r \rightarrow 0$ . We note that this cutoff has no other effect on the  $q$  dependence of eq 4.

The Fourier transform of the  $|\nabla \mathcal{M}|^2$  term yields a positive contribution that is proportional to  $q^2 \mathcal{M}_q^2$ , whose minimum is always attained for  $q = 0$  (uniform state). However, the dipolar–dipolar term in eq 4 favors short wavelength modulations (high  $q$  modes) due to the reduction in dipolar energy when the spin pair is in an antiparallel state. The combined free energy,  $\mathcal{F}_d + \mathcal{F}_{\text{GL}}$ , includes the direct exchange, eq 1, as well as the long-range dipole–dipole interactions, eq 4. Representing the total free energy as an integral in Fourier space, its minimization with respect to  $q$  gives the most stable mode,<sup>10</sup>  $q = q^*$

$$\begin{aligned} \frac{d}{dq} \left( \frac{\mu_0}{32\pi^3} G(q) + c q^2 \right) &= 0 \\ q^* &= -\frac{\mu_0 dG/dq}{64\pi^3 c} \approx \frac{\mu_0}{64\pi^3 c} g_1 > 0 \end{aligned} \quad (5)$$

In the derivation of  $q^*$  in eq 5, we neglected fourth and higher order terms in the free energy, eq 1. Estimating the free energy by its value at  $q^*$  is called the single-mode approximation. It can be justified for  $T \lesssim T_c$ , where the most dominant  $q^*$  mode contribution is a good approximation for the entire free energy.<sup>16</sup>

Note that for a single  $q$  mode, the domain size by definition is  $d^* = 2\pi/q^*$ . Up to a numerical prefactor, the domain wall width  $\xi$  is approximately equal to  $d^*$ . As the temperature is lowered and becomes considerably lower than  $T_c$ , the system cannot be described any longer within the single-mode approximation. Domains still prevail, but their wall width  $\xi$  (on order of nanometers) becomes much smaller than the domain size  $d^*$  (micrometers).

At low temperatures, an estimate of  $d^*$  includes many  $q$  modes and can be done for stripes, circular, and other simple arrangements of domains. By considering an alternating arrangement of  $\pm \mathcal{M}$  stripe domains, the dipolar energy, eq 3, can be calculated exactly. This energy competes with the domain

wall energy  $\gamma$ , which favors as few domains as possible. These two competing interactions<sup>10</sup> give in 2D

$$d^* = \frac{2\pi}{q^*} \approx a \exp\left[\frac{b\gamma}{2\mu_0\mathcal{H}^2}\right] = a \exp\left[\frac{b}{2}N_{B_0}^{-1}\right] \quad (6)$$

where  $a$  is a microscopic length and  $b$  is a dimensionless prefactor. The dimensionless number  $N_{B_0} = \mu_0\mathcal{H}^2/\gamma$  is called the magnetic Bond number and is also discussed in section VI. The same Bond number that fixes the domain size is also instrumental in providing an understanding of various instabilities of isolated drop-like domains, such as domain division and elongation, and tip splitting.<sup>1</sup>

### III. Magnetic Garnet Films

Garnet films are ferromagnetic solid films grown so that the easy axis of magnetization is along the axis of growth.<sup>6</sup> The magnetic spin can point up or down. Using polarized light microscopy coupled to the spin orientation (via the Faraday effect) to visualize details on the micrometer scale, it is observed that below the Curie temperature, the film spontaneously forms domains with a disordered stripe morphology [see Figure 1a]. It is quite evident that the stripe thickness (domain size) is well defined even though the stripes have no preferred orientation in the plane. Note that for larger external fields, the garnet film morphology changes into a bubble phase [see Figure 1b], as will be discussed below.

The physics behind the creation of domains in garnet films and, in particular, their preferred size  $d^*$  is well understood<sup>6,7,17</sup> and closely related to the model 2D layered system presented in section II. The major difference between the two is that the garnet film has a slab geometry of finite thickness  $t$ .

Any magnetized body of finite size produces magnetic charges or poles at its surface. This surface charge distribution, acting in isolation, is itself another source of a magnetic field, called the demagnetizing field. It is called the demagnetizing field because it acts in opposition to the magnetization that produces it. Consequently, the coarse-grained dipolar magnetic energy as in eq 3 can be calculated by mapping the system into a Coulomb interaction between two monolayers of opposite charges separated by a distance  $t$ . The kernel appearing in eq 3 is now replaced by<sup>17</sup>

$$g(r) \sim \frac{2}{r} - \frac{2}{\sqrt{r^2 + t^2}} \quad (7)$$

and the corresponding Fourier transform is

$$G(q) \sim \frac{4\pi}{qt}(1 - \exp(-qt)) \quad (8)$$

As in section II, the minimization of the free energy of eq 5 with the form of  $G(q)$  given by eq 8 yields an optimal value of the modulation wavevector,  $q^*$ . The connection between the finite thickness slab of the garnet and the 2D monomolecular dipolar layer can be seen by examining the  $qt \ll 1$  limit, where we find that  $G(q) \sim -|q|$  as in eq 4. In the other limit of a thick slab,  $qt \gg 1$ ,  $G(q) \sim 1/q$ , which also gives rise to a free-energy minimum at a nonzero value of  $q^*$ .

Stripe-like domains can be stabilized even for zero applied magnetic field, where there is a complete symmetry between

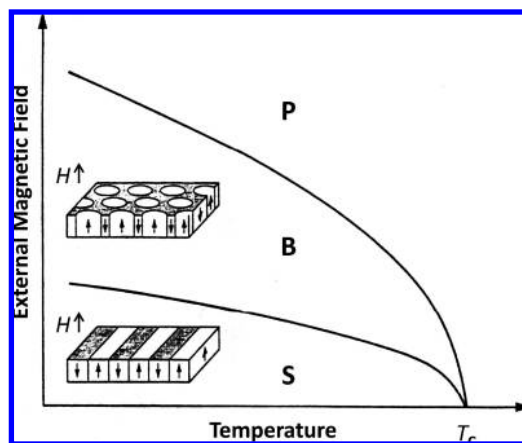


**Figure 2.** Schematic phase diagram of modulated phases (garnet films). The 2D system exhibits stripe (S) and bubble (B) phases, along with the usual paramagnetic (P) phase in the temperature–field ( $T$ – $H$ ) plane. The lines indicate first-order transition lines from S to B and then from the B to P phase. Both lines merge at the Curie point  $T_c$  for  $H = 0$ . Also indicated is the geometry of the stripe and bubble arrays for magnetic garnet films. Arrows indicate the magnetization direction.

the up and down spin orientations. In a slab of thickness  $t$  in the micrometer range, the resulting demagnetizing fields are strong enough to compete with the magnetic wall energy and yield stable stripe-like domains with size  $d^*$  in the 1–100  $\mu\text{m}$  range. Beside its dependence on the slab thickness  $t$ , the stripe width  $d^*$  depends on the temperature.

A typical phase diagram of a garnet film<sup>17</sup> is shown schematically in Figure 2 and depends on the temperature and external magnetic field (for a fixed slab thickness  $t$ ). For  $H = 0$ , the up and down stripes are completely symmetric. When an external field is applied below the Curie temperature, the domains whose magnetization is parallel to the field direction grow at the expense of the oppositely oriented domains. However, at some value of  $H$ , there is a first-order phase transition between the stripe morphology (S) and the so-called bubble phase (B), as seen in Figure 2. The bubble phase is composed of thin cylinders of up spin embedded in a background of down spins. Upon further increase of the magnetic field, the system has another first-order phase transition from the bubble phase into a paramagnetic (P) phase. Note that the two transition lines,  $S \rightarrow B$  and  $B \rightarrow P$ , terminate at the Curie temperature  $T_c$  for  $H = 0$ . Although the periodicity is, by and large, determined by such equilibrium considerations, the system shows a wide range of in-plane disorder [Figure 1a and c]. This disorder is very sensitive to the sample history, indicating that care be taken to avoid trapping the system in metastable states. A sample cooled in a nonzero  $H$  field which is then removed shows different disorder compared with a sample annealed at the same temperature but at zero magnetic field.

Garnet films had their days of glory in the 1960s and 1970s when they were used as magnetic storage devices (bubble memory), but their larger size and slower speed compared to hard disk drives and flash memory devices made this application short-lived.<sup>7,18</sup> However, even current research<sup>8</sup> on meso- and nanomagnetism is largely inspired by the garnet films.

### IV. Dipolar Langmuir Films

Amphiphilic molecules have a hydrophobic tail and a hydrophilic head that is either charged or dipolar. When these molecules are highly insoluble in the water, they form a Langmuir monolayer — a monomolecular layer that is spread



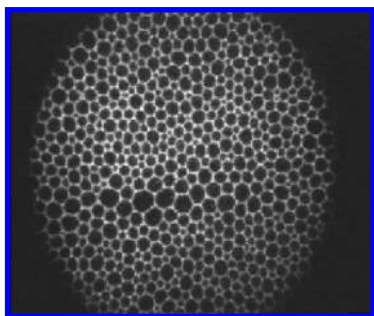


**Figure 3.** Fluorescence microscopy of alkyl lipid monolayers at  $T = 20^\circ\text{C}$  and area per molecule of  $60\text{\AA}^2$  showing 2D gas–liquid coexistence. The outer circle has a diameter of  $\sim 240\text{ }\mu\text{m}$ . Adapted from ref 22.

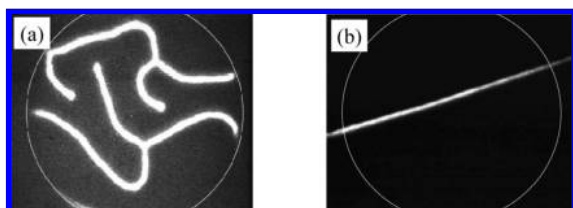


**Figure 4.** (a) Partially fluoro-alkylated lipid monolayers at the same temperature and with an area per molecule of  $97\text{\AA}^2$  showing stripe-like domains with a stripe thickness of around  $5\text{--}8\text{ }\mu\text{m}$ . (b) Same setup as that in (a) but with the addition of  $0.1\text{ mol}\%$  of cholesterol. A noticeable thinning of the stripe is seen to about  $\sim 1\text{--}3\text{ }\mu\text{m}$ . The outer circle has a diameter of  $\sim 240\text{ }\mu\text{m}$  in both figure parts. Adapted from ref 22.

at the air–water interface.<sup>19</sup> The layer thermodynamics can be controlled by regulating the temperature or applying a surface (in-plane) pressure. Visualization of domains in the micrometer range is accomplished by fluorescence optical and Brewster angle microscopies,<sup>20</sup> while ordered lipid domains are studied using small-angle X-ray scattering (SAXS).<sup>21</sup>

Such a Langmuir monolayer can be viewed as a manifestation of a 2D layer of dipoles at the water–air interface<sup>9,10,20</sup> whose surface density can be varied by applying a surface pressure. Although the dipoles are electric ones, the treatment of the long-range dipole–dipole interaction is similar to the one discussed in the preceding sections for dipoles having a nonzero contribution along the perpendicular  $z$  direction. We simply need to replace the magnetic field by an electric one and the magnetization by the electric polarization. The variation in the polarization  $\mathbf{P} = P\hat{\mathbf{z}}$  is related to the variation in the local concentration,  $P = \mu_{\text{el}}n$ , where  $P$  is the polarization,  $\mu_{\text{el}}$  the electric dipole moment of an individual molecule and,  $n(r)$  the local number concentration of dipoles (per unit area). One predicts various thermodynamic states of the system as a function of temperature  $T$  and lateral pressure  $\Pi$ , in analogy with the gas, liquid, and solid phases in 3D systems.

When the molecular dipole is large, the selection of a preferred domain size can be largely attributed to the competition between dipolar interactions and the domain line tension  $\gamma$ . This selection is analogous to the pattern selection, as discussed in the previous two sections. For example, we show in Figure 3 the domain structure of an alkyl lipid forming a Langmuir monolayer<sup>22</sup> and in Figure 4a the fluoro-alkylated lipids where most of the alkyl groups are replaced by fluorinated ones. Due to the large dipole associated with the  $\text{CF}_3$  chain extremity, the domain size of the fluorinated lipids is much smaller than that of hydrogenated lipids.

We mention one set of experiments that indicate that the observed patterns are due to an equilibrium  $q$  mode selection,

as we have discussed. In a Langmuir monolayer formed by the phospholipid DPPC,<sup>20</sup> liquid-crystalline domains are seen. They take the shape of a network of elongated stripe-like structures embedded in a liquid-like background. It is known that cholesterol preferentially adsorbs to the domain perimeter and reduces the line tension  $\gamma$  between the domains and their liquid-like background.<sup>20</sup> Indeed, when cholesterol was added to the DPPC monolayer, the system quickly reduced the domain width to another characteristic width. This experimental observation is in accord with the theoretical prediction, eq 6, where a reduction in  $\gamma$  strongly reduced the size of  $d^*$ . The effect of cholesterol was also studied for fluorinated lipids in ref 22. Addition of a small amount of  $0.1\text{ mol}\%$  of cholesterol thins the fluoro-alkylated stripes by a large factor, as can be seen in Figure 4b.

Some of the problems in understanding the thermodynamics of Langmuir monolayers are related to their slow kinetics. In some cases, it is not clear whether the system reached its equilibrium state or was trapped in a long-lived metastable one. Thus, although dipoles play an important role in determining domain size and morphology, their precise role is not fully understood.

## V. Block Copolymers

We depart from 2D systems and consider now extensions to 3D modulations occurring in block copolymers (BCP). These are polymeric systems in which each polymer chain is composed of several homogeneous blocks. Block copolymers exhibit a fascinating variety of self-assembled nanoscale structures with various types of chain organization. We focus only on the simplest, linear A–B diblock chain architecture, in which a homogeneous and long polymer chain of type A is covalently bonded with a B chain.<sup>13,14,23–26</sup> Composite materials made by mixing two or more different types of polymers are often incompatible and undergo phase separation. Such macrophase separation is hindered in BCP systems due to the chain connectivity.

By properly choosing the polymer blocks, it is possible to design novel composite materials made of BCP chains with desired mechanical, optical, electrical, and thermodynamical properties.<sup>13</sup> For example, by joining together a stiff (rod-like) block with a flexible (coil) block, one can obtain a material that is rigid but not brittle. Moreover, the interplay between flexibility and toughness can be controlled by temperature. More recently, BCPs are being explored in applications such as photonic band-gap materials, dielectric mirrors, templates for nanofabrications, and in other optoelectronic devices.<sup>27,28</sup>

Liquid melts of block copolymers or BCP–solvent liquid mixtures form spatially modulated phases in some temperature range. As an example, we show in Figure 5 the multitude of modulated phases in the well-studied polystyrene–polyisoprene (PS–PI) block copolymer system.<sup>29</sup> The two important parameters that determine the phase diagram of the figure are the mole fraction of one of the two components,  $f_A$ , and the product of two parameters,  $N\chi_{AB}$ , where  $N = N_A + N_B$  is the BCP chain degree of polymerization (total number of monomers) and  $\chi_{AB} \sim T^{-1}$  is the Flory constant. The latter is a dimensionless parameter representing the ratio of the energy of interaction to the thermal energy  $k_B T$  and quantifies the relative interaction between the A and B monomers. Typical values of  $\chi_{AB}$  are small compared to unity (about  $\chi_{AB} \approx 0.1$  for styrene–isoprene).

At high temperatures (low value of  $N\chi_{AB}$ ), the BCP melt is in a disordered liquid state in which the different chains show no particular organization. As the temperature is reduced below

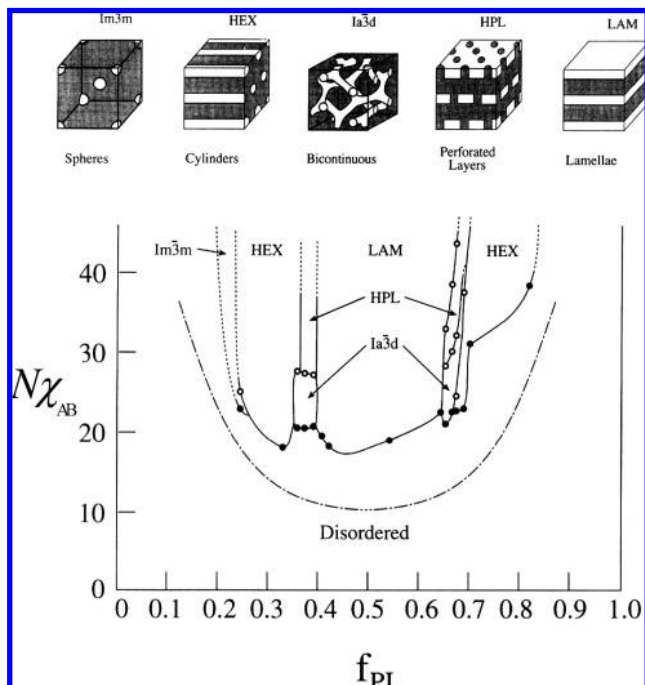


**Figure 5.**  $N\chi_{AB}$  versus  $f_{PI}$  phase diagram for PI-PS diblock copolymers, where  $f_{PI}$  is the mole fraction of the isoprene block. The dash-dot curve is the mean-field prediction for the instability of the disordered phase. Solid curves are experimental ones and have been drawn to delineate the different phases observed but might not correspond to precise phase boundaries. Five different ordered microstructures (shown schematically) have been observed for this chemical system. Adapted from ref 29.

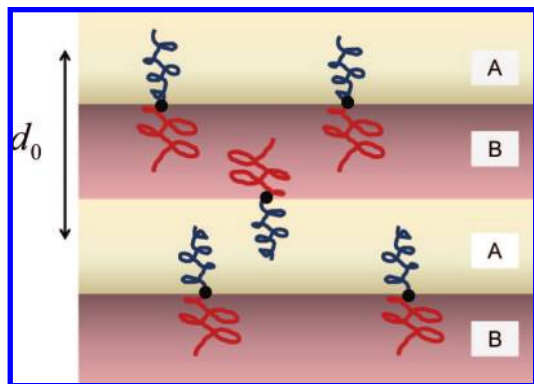


**Figure 6.** Schematic representation of a symmetric lamellar phase of di-BCP ( $f_A = 0.5$ ). The periodicity  $d_0$  is twice the thickness of each of the A and B lamellae.

some critical value ( $N\chi_c \approx 10.5$  in Figure 5), the partial incompatibility between the A and B blocks causes a microphase separation into one of several modulated phases. These so-called mesophases have spatial modulation in the 10–100 nm range and can have several symmetries. Figure 5 shows the lamellar (LAM), hexagonal (HEX), body-centered cubic (of group symmetry  $Im\bar{3}m$ ) and bicontinuous gyroid (of group symmetry  $Ia\bar{3}d$ ) phases, as well as a perforated lamellar phase (HPL) that is believed to be a long-lived metastable state but not a true, thermodynamic stable phase.

**A. Modulated Periodicity in BCP.** How can we understand the self-assembly and stability of various BCP modulated phases with definite periodicity? While sophisticated theories<sup>24,30–37</sup> quite successfully reproduce complex phase diagrams such as Figure 5, we present here a qualitative and heuristic explanation.<sup>23</sup> Consider a symmetric diblock copolymer ( $f_A = N_A/N =$

0.5) whose structure is that of a lamellar stack as depicted in Figure 6. The unidirectional periodicity  $d$  is taken as a parameter, and its value will be determined later. We also assume that the two blocks have the same monomer size,  $a$ . If the A and B chains were not connected, the coarsening that usually occurs during phase separation would result in a macrophase separation (theoretically with  $d \rightarrow \infty$ ). However, as the BCP periodicity  $d$  increases, the A–B chains start to stretch and lose entropy. The competition between coarsening and chain entropy results in a preferred domain size  $d$ ; this is a characteristic of all BCP systems.

For a lamellar phase with  $f_A = 0.5$ , the free energy per copolymer chain can be written as a sum of two terms

$$f_{\text{chain}} = k_B T \frac{3(d/2)^2}{2Na^2} + \sigma \Sigma \quad (9)$$

The first term expresses the entropy cost of stretching an ideal chain (similar to a Gaussian random walk) of  $N$  monomers to span half of the lamellar period,  $d/2$ , from its unperturbed size  $aN^{1/2}$ . The second term is the interfacial energy per chain where  $\sigma \sim \chi_{AB}^{1/2}$  is the surface tension (in units of energy per area), and  $\Sigma$  is the area per chain at the A/B interface. Because we consider a diblock polymer melt (i.e., with no solvent), the system is assumed to be incompressible; the volume occupied by each chain is fixed,  $v_{\text{chain}} = Na^3 = \Sigma d/2$ , where  $a^3$  is the volume of one monomer. Substituting the incompressibility condition,  $\Sigma \sim d^{-1}$ , into eq 9, the chain free energy is minimized with respect to the lamellar thickness  $d$ , whose optimal value is

$$d_0 \approx 1.39 \left( \frac{\gamma_{AB} \sigma a^2}{k_B T} \right)^{1/3} a N^{2/3} \sim \chi_{AB}^{1/6} N^{2/3} \quad (10)$$

where we used the simple scaling dependence of  $\sigma$  on  $\chi_{AB}$ . Hence, from a simple free-energy minimization, we find that the lamellae have a preferred periodicity  $d_0 \sim N^{2/3}$  that scales as the two-thirds power of the BCP molecular weight; this should be compared with the unperturbed size  $\sim N^{1/2}$ . Hence, this means that the BCP chains in a lamellar phase are highly stretched due to their partial incompatibility. The prediction of novel structures using a simple free-energy minimization subject to structural and composition constraints is an essential element behind the more refined theories<sup>24</sup> and is characteristic of all BCP systems.

#### B. Orientation of Anisotropic Phases by an Electric Field.

As noted previously, block copolymers form heterogeneous composite materials. Since most polymers are nonconducting dielectrics, a modulated phase of BCP is a heterogeneous dielectric, with a spatially varying dielectric constant that depends on the dielectric constants of the two blocks,  $\epsilon_A$  and  $\epsilon_B$ . When an anisotropic BCP phase (such as a lamellar stack or a hexagonal arrangement of cylinders) is placed in a strong enough external electric field  $E$ , the most apparent effect is an orientation of the BCP domains in the direction of the external field.<sup>38–48</sup> The term in the free energy accounting for this effect is proportional to  $(\epsilon_A - \epsilon_B)^2 E^2$ . In coarse-grained models of BCP melts, only the local relative A/B concentration is retained. It is represented by a continuous composition variable,  $\phi(\mathbf{r})$ , that varies between 0 (pure B) and 1 (pure A). The dielectric constant can be taken as a linear interpolation of the local composition  $\phi$ ,  $\epsilon(\mathbf{r}) = \phi(\mathbf{r})\epsilon_A + (1 - \phi(\mathbf{r}))\epsilon_B$ , and its spatial average is  $\langle \epsilon \rangle = f_A \epsilon_A + (1 - f_A)\epsilon_B$ . In the weak segregation

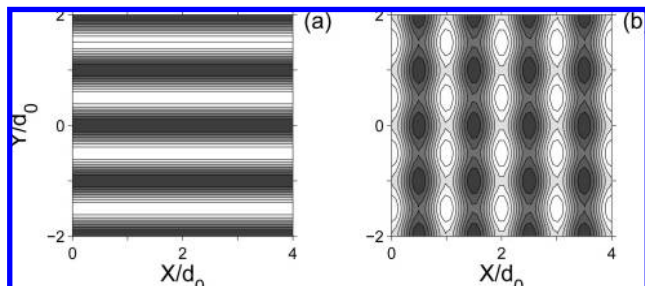


**Figure 7.** Calculated contour plots of a symmetric BCP lamellar phase between two planar electrodes and under an external electric field. The electrode surfaces are at  $y = \pm 2d_0$ , and the field is in the  $y$  direction. The B monomers (colored black) are attracted to both surfaces. (a) For an  $E$  field slightly smaller than the critical field,  $E = 0.98E_c$ , the film exhibits a perfect parallel ordering. (b) For an  $E$  field just above the threshold,  $E = 1.02E_c$ , the film morphology is a superposition of parallel and perpendicular lamellae. Adapted from ref 38.

limit ( $\chi_{AB} \approx \chi_c$ ), the electrostatic energy per unit volume was shown by Amundson and Helfand<sup>39</sup> to have the form

$$\frac{(\epsilon_A - \epsilon_B)^2}{2\langle\epsilon\rangle} \sum_{\mathbf{q}} \frac{(\mathbf{q} \cdot \mathbf{E})^2}{q^2} \phi_{\mathbf{q}} \phi_{-\mathbf{q}} \quad (11)$$

where the sum is taken over all Fourier modes,  $\phi(\mathbf{r}) = \sum_{\mathbf{q}} \phi_{\mathbf{q}} \cos(\mathbf{q} \cdot \mathbf{r})$ . Minimizing the sum of the electrostatic energy, eq 11, and the nonelectrostatic BCP free energy produces an orientation transition<sup>38</sup> shown in Figure 7. At a large enough  $E$  field, there is a first-order transition to a lamellar phase that is oriented in the direction parallel to the  $E$  field (the  $y$  axis in the figure). The modulations seen in Figure 7b are typical of the weak segregation limit and disappear for larger  $E$  fields. In other works, such electric field orientation was also reported for cylindrical phases.<sup>48,49</sup>

**C. Phase Transitions Induced by Electric Fields.** It is well-known that a drop of highly permeable ferrofluid placed in a strong magnetic field elongates into a prolate ellipsoid and then, via a first-order phase transition, sharply transforms into a needle-like drop.<sup>3</sup> This transition also occurs for charged or dipolar liquid drops.

Quite recently, a similar phenomenon was observed and modeled in bulk BCP systems.<sup>50–53</sup> The starting point is a cubic (bcc) phase of isolated spherical drops rich in one of the blocks (say A), embedded in a background of the other component (B). As can be seen in Figure 8, this situation occurs for asymmetric BCP ( $f_A \neq 0.5$ ). When such a cubic phase of spheres (bcc) is placed in an external  $E$  field, each of the spheres elongates in the same (111) direction of the  $E$  field (Figure 8a). As the value of the  $E$  field increases above a critical value  $E_c$ , the distorted cubic phase undergoes a first-order phase transition to a hexagonal phase of cylinders pointing also along the same  $E$  field direction, Figure 8b.

Using two different computational techniques,<sup>52</sup> the full phase diagram in the parameter space of  $f_A$ ,  $\chi_{AB}$ , and  $E$  can be calculated with semiquantitative agreement between the two methods. The resulting phase diagram for a fixed value of  $f_A = 0.3$  is shown in Figure 9. The distorted cubic phase has an  $R\bar{3}m$  group symmetry and undergoes a phase transition to a hexagonal phase (hex) or a completely disorder phase (dis) depending on the initial value of the Flory constant,  $\chi_{AB}$ . Although the full phase diagram has not yet been measured, some of the observations agree with the model presented here for the PS–PMMA (polystyrene–polymethylmethacrylate) system.<sup>50</sup>

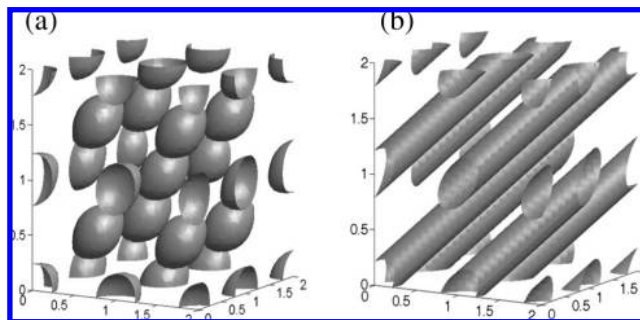


**Figure 8.** Contour plots of a BCP phase in an electric field with  $f_A = 0.37$  and  $N\chi_{AB} = 12$ . At zero  $E$  field, the stable phase is a cubic phase (bcc) (not drawn). (a) For  $E = 0.98E_c$ , just 2% below the critical field and oriented along the (111) direction of the lattice, each of the spheres deforms into a prolate ellipsoid, and the bcc phase changes continuously into a phase with an  $R\bar{3}m$  space group symmetry. (b) For  $E = 1.02E_c$ , just 2% above the critical field, the system undergoes a first-order phase transition into a hexagonal array of cylinders, also pointing along the  $E$  field direction. Adapted from ref 51.

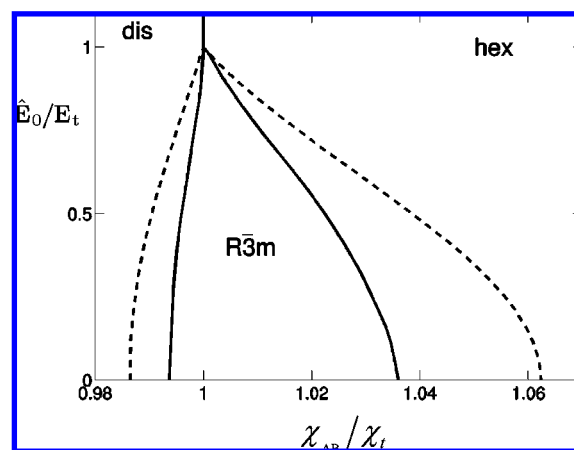


**Figure 9.** Phase diagram of block copolymers in an electric field, in the plane defined by the Flory constant  $\chi_{AB}$ , and the normalized electric field  $\hat{E}_0$  for  $f_A = 0.3$ . The distorted bcc phase, denoted by its space group symmetry as  $R\bar{3}m$ , is bounded by the hexagonal (hex) and disordered (dis) phases and terminates at a triple point where all three phases coexist. The solid line is the prediction of an analytical one-mode approximation, whereas the dashed lines are obtained by a more accurate, self-consistent numerical study. The axes are scaled by  $(\chi_t, E_t)$ , which are the values of  $\chi_{AB}$  and  $\hat{E}_0$  at the triple point. Adapted from ref 52.

We end this section by mentioning that mobile ionic impurities can have an important effect on the phase transitions and alignment of modulated BCP phases. This is an active field of current investigations.<sup>51,54</sup>

## VI. Ferrofluids and Their Composites

This section pertains to the magnetic fluids termed ferrofluids, suspensions of single-domain magnetic particles in a liquid carrier that are ultrastable against settling.<sup>3</sup> The prototypical ferrofluid is made up of magnetite ( $\text{Fe}_3\text{O}_4$ ) colloidal particles having a mean size (diameter) of 10 nm, coated with a 2 nm monolayer of oleic acid, and suspended in a hydrocarbon carrier fluid such as kerosene. Many surfactants in addition to oleic acid are known to produce stable ferrofluids in a wide variety of liquid carriers such as other hydrocarbons, aromatics, esters, alcohols, fluorocarbon, and water carriers. The particles are in rapid thermal or Brownian motion that prevents them from settling under gravity. Concomitantly, the particles collide with each other, and the coating prevents the particles from ag-



glomerating together and settling out. The particles are said to be sterically stabilized. Another class of water-based ferrofluids are ionically stabilized with electric double layers.<sup>55</sup>

A ferrofluid worthy of the name is free of the chaining that results from the magnetic attraction and adherence of magnetic particles to each other with an energy that exceeds that of thermal displacements. Chaining is a topic in which there is much confusion in the literature. Using the typical colloidal particle size of 10 nm and the magnetization of the usual magnetic particle magnetite, the mean number of particles in a chain computed from the de Gennes and Pincus theory<sup>56</sup> is 1.36 in a strong  $H$  field and 1.26 in zero field. Thus, the particles are essentially monodispersed. In simulations, the ferromagnetic particles are invariably taken to be larger and/or with stronger magnetic dipoles, resulting in particle chaining. The particle size does not have to be much larger than 10 nm before chaining becomes a practical problem in ferrofluids; at 13 nm, chains of magnetite are predicted to be infinite in length. The much larger (micrometers diameter) particles of a magnetorheological (MR) fluid chain easily, which is the basis for their entirely different applications.<sup>57–59</sup>

Ferrofluids based on elemental ferromagnetic particles of iron, nickel, cobalt, and their alloys oxidize after days of contact with the atmosphere and are not suitable for long-term use, except in sealed systems. However, other magnetic solids such as maghemite ( $\text{Fe}_2\text{O}_3$ ) and mixed metal ferrites yield ferrofluids that are long-term stable against oxidation in contact with the atmosphere.

Due to the nanometer size colloidal particles, thermal fluctuations are a governing influence in the behavior of ferrofluids. Accordingly, statistical mechanical analysis permits computation of the magnetization law and other physical properties. This stands in contrast, for example, to the behavior of magnetorheological fluids containing particles in the micron size range which aggregate together when subjected to an applied magnetic field and require mechanical force to become redispersed. Flow of magnetic fluid in a magnetic field is subject to polarization force and constitutes a discipline in itself (ferrohydrodynamics), comparable to but distinct from magnetohydrodynamics, that is, the flow of conductive, nonmagnetic fluid (such as molten metals) in the presence of magnetic fields. An introduction to the science with an extensive treatment of the effects of flow fields is found in the monograph of Rosensweig.<sup>3a</sup>

Figure 10 is a schematic illustration of six types of fluid systems containing magnetic particles. Four out of the six, (a), (b), (c), and (e), include ferrofluid as a component. Black particles indicate single-domain magnetic particles having size on the order of 10 nm, typical of particles in a stable ferrofluid, that is, one which remains free of chaining of particles whether subjected to an applied magnetic field or not. Gray denotes multidomain magnetic particles, and white denotes particles that are nonmagnetic. Modulations (e.g., formation of particle chains) can take place when the composites are subjected to an applied magnetic field. A discussion of systems (d) and (f) can be found in ref 3c.

**A. Modulation of Ferrofluid Interfaces.** Ferrofluids exhibit a number of unique interfacial instabilities. These are phenomena occurring in ferrofluids of uniform temperature and colloidal composition. The number density of particles is on the order of  $10^{23}$  per cubic meter (Avogadro number); hence, the ferrofluid can be considered a continuum for most purposes. The modulations can be grouped into categories. Except where cited, the phenomena listed below are discussed in detail in ref 3a.

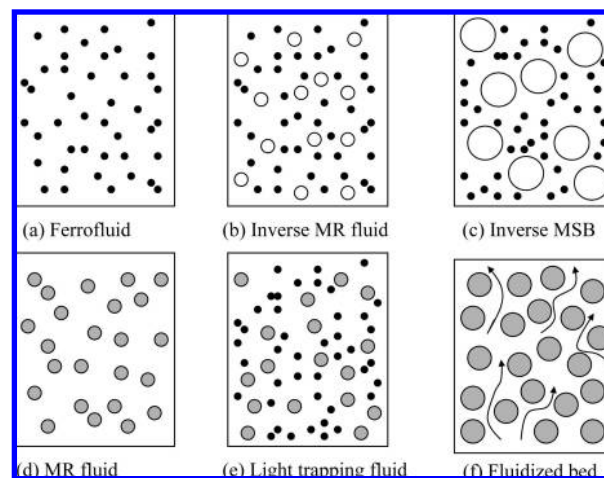


**Figure 10.** Classification of particle suspensions in a fluid carrier prior to modulation by an applied magnetic field. (a) Nanometer single-domain magnetic particles in a nonmagnetic carrier; (b) nonmagnetic micrometer size range particles in a matrix of ferrofluid; (c) nonmagnetic millimeter particles in ferrofluid; (d) multidomain magnetic particles in nonmagnetic carrier fluid; (e) multidomain magnetic particles in ferrofluid; (f) multidomain magnetic particles suspended in a flowing stream of gas or liquid. MR denotes magnetorheological. MSB denotes magnetically stabilized (fluidized) bed. Particles indicate the ordering of sizes only.

Cases when a uniform, steady, magnetic field is applied to motionless ferrofluid include (i) the normal-field instability, (ii) prevention of Rayleigh–Taylor instability, (iii) stabilization of a fluid column, (iv) droplet shape modulation, and (v) labyrinthine patterning. Cases with uniform, steady, magnetic field applied to ferrofluid in motion include (i) modulation of Kelvin–Helmholtz instability and (ii) modulation of Saffman–Taylor instability. In another category, we mention modulations in a time-varying magnetic field.<sup>60,76</sup>

Additional modulations occur in ferrofluids supporting a temperature gradient when the magnetization is temperature-dependent. Studied cases include (i) convection of a plane layer in uniform applied magnetic field, (ii) convection of a plane layer in a constant magnetic field gradient, and (iii) convection in a spherical system with a radial magnetic field gradient.<sup>61</sup>

The above is not an exhaustive list as systems can be rotated, the concentration can be nonuniform, various instabilities can be combined, and so forth. In addition, in all of the systems listed, the magnetization is equilibrated and hence is collinear with the applied field. In comparison, in systems where the ferrofluid is subjected to rapid change in direction and magnitude of the applied field, the magnetization lags the field, which excites additional forces. Modulation in this latter category is virtually unexplored.

Most studied is the normal-field Rosensweig instability; see Figure 11. Accordingly, after a brief introduction, we highlight a selection of related works, many of which are concerned with nonlinear aspects of this patterning phenomenon.

**B. Normal-Field Instability.** This is the first instability of a ferrofluid to be observed; it is striking, and it is the best known. Peaks form in a patterned array on the free surface of a pool of ferrofluid exposed to a uniform, vertically oriented magnetic field. This pattern persists under static conditions, in contrast to patterns such as Bénard cells produced in dissipative systems far from equilibrium.

The ferrofluid pattern is sustained as a conservative system, that is, in the absence of energy input or dissipation. The patterning can only onset in a ferrofluid having a magnetization

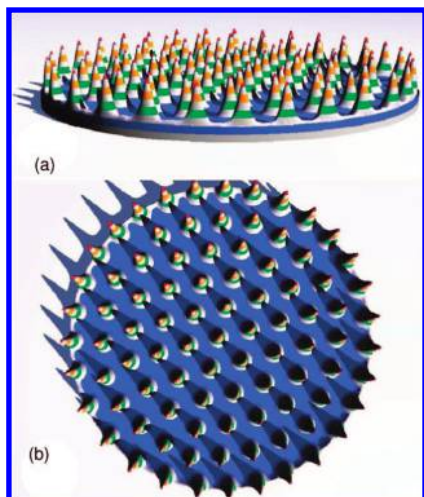


**Figure 11.** Surface relief of normal-field instability of a ferrofluid reconstructed from X-ray images. (a) Oblique view. Each layer of a peak having a given color represents 1 mm of thickness; (b) plane view. The containing vessel is 12 cm in diameter, and the initial liquid depth is 3 mm. Adapted from ref 62.

that exceeds a critical value and was never seen until a ferrofluid having a sufficiently high magnetization was synthesized.<sup>63</sup> The instability in its pristine form is realized in a horizontal pool of ferrofluid subjected to a uniform, vertically oriented magnetic field. The linear analysis and experimental validation were given by Cowley and Rosensweig,<sup>64</sup> valid for a ferrofluid having magnetization nonlinearly dependent on the magnetic field  $H$ . The critical magnetization  $M_c$  is specified in dimensionless form by

$$\frac{\mu_0 M_c^2}{\sqrt{g \Delta \rho_m \sigma}} = 2 \left( 1 + \frac{1}{r_p} \right) \quad (12)$$

where  $\mu_0$  denotes the permeability of vacuum,  $g$  the gravitational constant,  $\Delta \rho_m$  the difference in mass densities of fluids across the interface,  $\sigma$  the interfacial tension, and  $r_p$  the dimensionless permeability ratio

$$r_p = \left( \frac{\mu_0 \mu_t}{\mu_0^2} \right)^{1/2} \quad (13)$$

For the nonlinear medium, the parameter  $r_p$  depends on two permeabilities at the operating point, the chord permeability  $\mu_c = B(H)/H$  and the tangent permeability  $\mu_t = \partial B(H)/\partial H$ . Although the onset of instability depends crucially on the magnetic field via the critical magnetization  $M_c$ , the spacing between peaks  $\lambda$  at the onset is independent of the magnetization and is given by

$$\lambda = 2\pi \left( \frac{\sigma}{g \Delta \rho_m} \right)^{1/2} \quad (14)$$

which is simply the capillary length between the two fluids. Note that it is the same as the wavelength at onset of ordinary Rayleigh–Taylor instability.<sup>3</sup>

It is instructive to indicate the physics of the normal-field instability in a simple way. The onset of the instability is governed by two conditions; (i) the undulating surface has the

same energy as the free surface at the point of onset, and (ii) its energy is minimized at the onset.

The total energy is the sum of surface, gravitational, and magnetic terms. We will consider the energies associated with a wave train of sinusoidal form,  $h(x) = \delta \cos(2\pi x/\lambda)$ , where  $\lambda$  is the wavelength and  $\delta$  is the amplitude of the disturbance, assumed small.

The surface energy is proportional to the surface area. Distance along the surface between crests is given by  $s \approx \lambda + (\pi\delta)^2/\lambda$ . The length along the unperturbed interface is  $\lambda$ ; hence, the perturbation of surface energy is given by  $\sigma(\pi\delta)^2/\lambda$ , where  $\sigma$  is the surface tension.

The perturbation of gravitational energy along a wavelength corresponds to the work done in lifting ferrofluid from the trough region to the crest region. This is given by the product of the lifted fluid volume  $\lambda\delta/\pi$  with the mass density difference of the ferrofluid  $\Delta\rho_m$ , the distance between the centroids  $\pi\delta/4$ , and the gravitational acceleration  $g$ . Thus, the gravitational term is  $\lambda\rho_m\delta^2g/4$ .

Rigorous formulation of the magnetic energy requires a separate computation of the magnetic field distribution to determine the energy density given by difference of the integral of  $HdB$  over the system volume, before and after the perturbation of the surface form. Magnetic energy density is reduced in a region occupied by the permeable ferrofluid as the fluid is more easily magnetized than empty space. Thus, because magnetization increases at the peaks of the waveform and decreases at the troughs, the overall magnetic energy decreases with the formation of peaks and tends to offset the concomitant increase in gravitational and surface energies. At a critical value of magnetization, the sum of the energies changes sign, and instability onsets.

Here, we assume that the energy term depends on magnetic permeability of free space  $\mu_0$ , magnetization  $M$ , and wave amplitude  $\delta$ . From dimensional consideration, the magnetic term is thus expressed as  $-\alpha\mu_0 M^2 \delta^2$ , where  $\alpha$  is a proportionality factor, and the negative sign (see section 3.6 of ref 3a) corresponds to the reduction in field energy attendant to an increase of magnetization. Adding the three energy terms and factoring out  $\delta^2$  yields

$$\sigma\pi^2/\lambda + \lambda\Delta\rho_m g/4 - \alpha\mu_0 M^2 = 0 \quad (15)$$

The equality follows from the first governing condition. Differentiation with respect to  $\lambda$  and rearranging yields the result of the second governing condition in the form

$$\lambda = 2\pi \sqrt{\frac{\sigma}{g \Delta \rho_m}} \quad (16)$$

This is the expression for spacing between the peaks, the same as that given by eq 14. Note that if  $\lambda$  were introduced along with or in place of  $\delta$  in the dimensional analysis, eq 16 would contain a dependence of  $\lambda$  on  $\delta$ . This would be wrong because  $\delta$  is of arbitrary size. Substituting for  $\lambda$  in the previous equation yields the relationship for the intensity of magnetization required for onset to occur.

$$\frac{\mu_0 M_c^2}{\sqrt{g \Delta \rho_m \sigma}} = \frac{\pi}{\alpha} \quad (17)$$

Comparison with eq 12 shows that  $\pi/\alpha = 2(1 + r_p)/r_p$ .



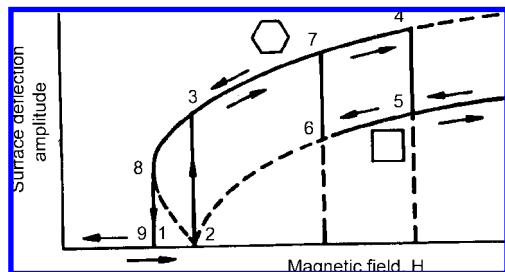


**Figure 12.** Schematic illustration of transformations in the normal-field instability according to Gailitis.<sup>66</sup> Field intensities from 1 to 2 are in the subcritical range; 2 is the onset field predicted by linear analysis; 2 to 3 represents the hard transition to the hexagonal array of peaks; 4 to 5 depicts transition to a square array. Two regions of hysteresis can be seen on the curves. In decreasing field, 8 is known as the turning point. Adapted from ref 3.

It is of interest to note that the onset of the normal-field instability of a ferrofluid bears analogy to the hexagonal patterns seen by direct observation in the transition of type-II superconductors.<sup>65</sup>

In an incisive study, Gailitis,<sup>66</sup> using an energy method to investigate nonlinear aspects of the patterning, showed that the instability is subcritical, that is, onset could occur at a lower value of applied field provided the disturbance is sufficiently large, while at the critical point, the onset is hard, that is, the surface deformation onsets as a jump rather than in a continuous manner. In addition, the prediction was made that the pattern, which onsets as a hexagonal array, can transform to a square array at higher applied magnetic field and that both transitions exhibit hysteresis. Some doubt remains, however, as the analyses are restricted to small values of the relative permeability. Subsequently, however, numerical analysis<sup>67</sup> using the Galerkin finite element method confirmed the subcritical character of the instability and correctly predicted experimentally measured heights of the peaks, while conditions for the transition from hexagons to squares was studied by Abou et al.<sup>68</sup> The sketch of Figure 12 illustrates the predictions of Gailitis.

More recently, interesting work has focused on the question of the shape and size of the peaks under various conditions. The most successful experimental results are obtained using the attenuation of X-rays directed vertically through the pool of ferrofluid.<sup>62</sup> In Figure 11, which displays the usual array of peaks over the entire surface, each color indicates a layer thickness of 1 mm. This technique was applied<sup>69</sup> to study the surface shape generated by a local perturbation in the first subcritical hysteretic regime of the instability. This is the regime identified as 1–2–3–8–1 in Figure 12. The perturbation is generated on a flat area of the fluid surface using a pulse of field from a small air coil placed below the center of the vessel. A single pulse produced a single peak of the hysteretic regime, and additional pulses generated additional peaks. A remarkable fact is that the peaks remain present after the pulse field is removed. The peaks are termed solitons by these authors (although solitons are generally understood to refer to nonlinear traveling waves that can pass through others with no loss of form). These soliton peaks self-organize into molecule-like clusters of 2, 3, 4, 5, 6, and more peaks in symmetric arrays. Figure 13 illustrates a pattern of nine solitons.

Figure 14 illustrates the distribution of the magnetic field and the cusped shape of a peak in a hexagonal array in the normal-field instability as determined by a numerical computation. The concentration of the field and attendant increase in the normal stress difference across the interface is mainly responsible for the formation of the peaks.



**Figure 13.** Nine solitons (solitary structures), each generated by a transient, local pulse of magnetic field applied in the subcritical range 1–2 of Figure 12. Peaks along the rim of the container are an artifact due to the curved surface of the meniscus. The containing vessel is 12 cm in diameter, and the liquid depth is 3 mm. Adapted from ref 69.

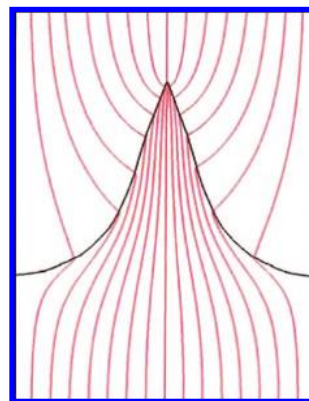


**Figure 14.** Finite element computation of the ferrofluid peak shape in the range 3–4 of Figure 12 using  $\mu/\mu_0 = 30$ . Adapted from ref 71.

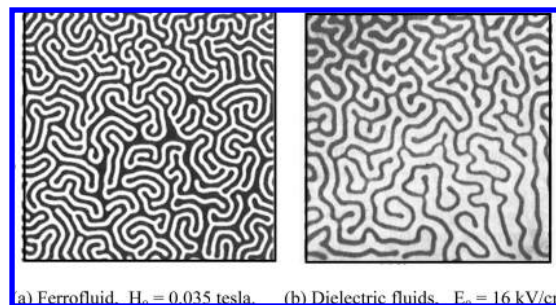


**Figure 15.** (a) The magnetic field applied to the ferrofluid and (b) the electric field applied to the dielectric oil yield labyrinthine patterning. Photos are 7 cm<sup>2</sup>. Adapted from ref 4.

Petrelis et al.<sup>70</sup> experimentally demonstrated the parametric stabilization of the normal-field instability of a ferrofluid using vertical vibrations of the fluid container. The measurements were in good agreement with an analytical model.

**C. Labyrinthine Instability in Polarized Fluids.** Labyrinthine instability of a ferrofluid shown previously in Figure 1c is shown again in Figure 15a alongside its dielectric dual in Figure 15b. The ferrofluid is contained between closely spaced horizontal glass plates (Hele–Shaw cell) together with an immiscible nonmagnetic fluid that preferentially wets the glass allowing a clear view of the pattern. A magnetic field is applied normal to the cell faces producing a pattern of stripes. The system is governed by the interaction between magnetic dipolar and interfacial energies.<sup>4</sup> Because thinner stripes have a fixed

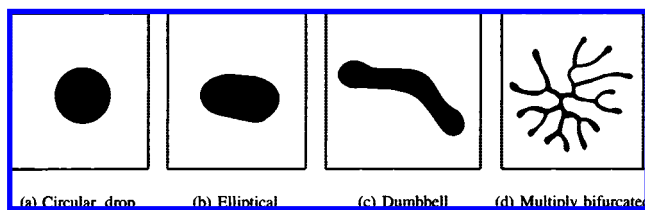


**Figure 16.** Experimental transition of a circular cylindrical drop of ferrofluid in response to increasing magnetic field. Adapted from ref 72.

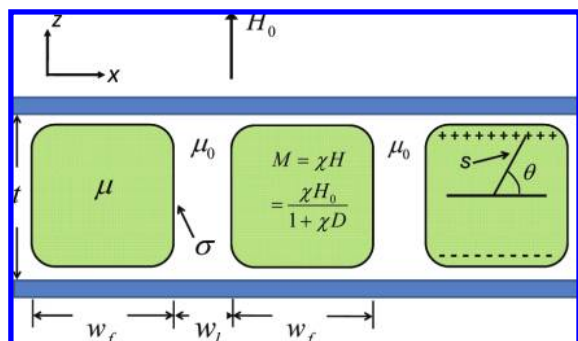


**Figure 17.** The labyrinth (see Figure 1c) modeled as a periodic system of infinitely long and parallel stripes in the  $x$  direction, alternating between ferrofluid stripes with permeability  $\mu$ , magnetization  $M$ , and width  $w_f$ , and nonmagnetic fluid stripes of width  $w_l$  and permeability  $\mu_0$ . The system has a thickness  $t$  in the  $z$  direction, which coincides with the direction of the applied field  $H_0$ . The interfacial tension between the two fluids is  $\sigma$ .

extent between the cell faces, they possess a smaller demagnetizing field, resulting in a higher magnetization and a further reduction in magnetic energy. Concomitantly, the thinner stripes present a larger interfacial area and, hence, a larger interfacial energy, which limits formation of ever thinner stripes.

Dielectric fluids are polarizable just as ferrofluids are magnetizable, and their response to applied electric fields, provided that free charge is absent, is analogous mathematically and physically to the response and patterning of the ferrofluids. Although the high intensity of the requisite applied electric field tends to be difficult to achieve, a successful implementation is shown in Figure 15b using lubricating oil (dark) paired with castor oil (transparent) in a specially insulated Hele–Shaw cell. An applied electric field of frequency 500 Hz ensured the absence of free charge, while the insulation ensured similarity of field boundary conditions at the interface between the fluids and the electrodes.

It should be noted that just as the magnetic garnet stripes in Figure 1a are analogous to the ferrofluid stripes in Figure 15a, the stripe domains of the dipolar Langmuir monolayer shown in Figure 4a are closely analogous to the dielectric labyrinth seen in Figure 15b. As implied previously, the magnetic systems are dual to the electric systems.

Figure 16 illustrates stages of the onset of a related phenomenon when only a small amount of ferrofluid (a drop) is put into the cell. Numerical analysis has been successful in producing realistic simulations. In one approach, the dipolar energy of the system is formulated as a function of its boundary.<sup>73</sup> Another approach writes the free energy in terms of particle concentration expressed as a Ginzburg–Landau expansion similar to eq 1 and combines these terms with a formulation expressing the surface energy.<sup>74</sup> The latter study predicts a further transformation of the labyrinthine pattern into a bubble array when a rotating in-plane magnetic field is

superposed on the steady, perpendicular magnetic field. Different patterns are formed depending on which field is applied first.<sup>60</sup>

In a vertically oriented cell, the two fluids form one layer over the other due to their difference in mass density, with the ferrofluid on the bottom when it is the denser. The flat interface between the fluids undergoes a transition that, in addition, depends on gravitational energy.<sup>3,63</sup> A linearized theory predicts the onset condition,<sup>72</sup> and the same authors present experimental photographs of the early onset terming the behavior “comb” instability. The highly convoluted labyrinthine patterns generated in a vertical cell subjected to higher applied fields are shown in ref 63.

A model stripe system is depicted in Figure 17. Two glass plates with a spacing of  $t$  in the  $z$  direction (Hele–Shaw cell) bound an immiscible mixture of a ferrofluid and another nonmagnetic fluid. In the model, the two fluids are assumed to form a periodic pattern of infinitely long and straight stripes. The ferrofluid stripes have a width of  $w_f$  in the  $x$  direction, while the nonmagnetic ones are of width  $w_l$ . The total energy per cycle is a sum of magnetic and fluid interfacial energies,  $U = U_m + U_\sigma$ , where the interfacial energy  $U_\sigma = 2\sigma t$  depends on the interfacial tension  $\sigma$  and the magnetic energy is given by

$$U_m = -\frac{1}{2}\mu_0 \int_V M H_0 dV = -\frac{\mu_0 \chi H_0^2 t w_f}{2(1 + \chi D)} \quad (18)$$

Thus, the energy per unit length along the interfacial direction is given by  $U/(w_f + w_l)$ .

The problem reduces to calculating the magnetization  $M = \chi H = \chi H_0 / (1 + \chi D)$  inside of the magnetic stripes of finite cross section, where  $\chi$  is susceptibility and  $D = (H_0 - H)/M$  is the demagnetization coefficient. In this system with putative spatially uniform magnetization, the volume density of poles disappears, and only surface poles remain. The demagnetization field of the surface poles is then computed from integration of the Coulomb expression for an infinitely long stripe,  $-M \sin \theta dx / 2\pi s$ , where  $s = [x^2 + (t/2)^2]^{1/2}$  is distance from the pole,  $x$  is the in-plane distance coordinate, and  $\theta$  is angle subtended between  $s$  and the  $x$  coordinate (see Figure 17).

The integration generates an infinite series of terms due to contributions from opposite poles of all of the stripes. Minimization of the total energy per unit length yields the governing expression for normalized stripe width  $W = w_f/t$

$$\frac{\chi^2 N_{B_0}}{(1 + \chi D)^2} \frac{\partial D}{\partial W} - \frac{2}{W^2} = 0 \quad (19)$$

and the magnetic Bond number,  $N_{B_0} = \mu_0 H_0^2 t / 2\sigma$ , introduced above in section II is the ratio of the magnetostatic energy to the interfacial energy. Computation shows that the stripe width decreases with increasing applied magnetic field  $H_0$  and susceptibility  $\chi$ .

Experiments in which wall spacing and applied field were systematically varied yielded stripe thicknesses in reasonable agreement with theory over a three decade range of the magnetic Bond number.

Figure 18 illustrates the influence of the container geometry on the patterning of labyrinthine instability.<sup>75</sup> The comb pattern that develops in the Hele–Shaw cell is replaced by the spiraling finger of the fluid.

The normal-field instability sets a limit on certain applications where it is desired that the ferrofluid maintain a smooth surface.

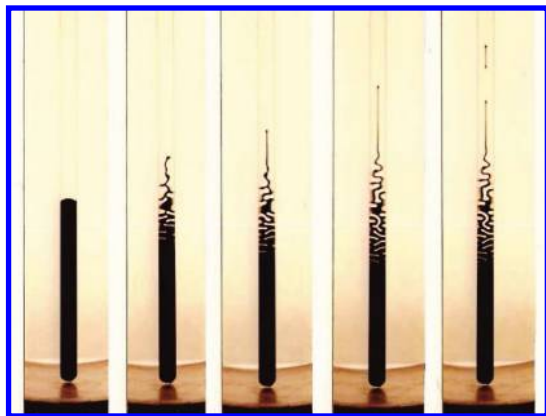


**Figure 18.** Spiral interfacial instability resulting from the tangential field applied to a column of ferrofluid in a capillary tube.<sup>75</sup> The magnetic field increases from left to right. Note the rupture of continuity at the highest field.

An illustrative example is the use of ferrofluid to produce inexpensive and versatile mirrors for astronomical optics and other uses.<sup>77</sup> The application has been intensely studied and found to be feasible. A reflective colloidal film of silver particles is spread on a ferrofluid and forms a mirror surface. The surface can be shaped by the application of a magnetic field to yield adaptive mirrors. Local regions of the surface can be shaped in real time by application of magnetic fields to yield adaptive mirrors that compensate for atmospheric disturbances of refractive index that, otherwise, cause twinkling of stars and reduction of the resolution of images. The shape can be rapidly varied in time with surface vertical displacements ranging from nanometers to several millimeters. Magnetization of the ferrofluid must be kept within limits to avoid the formation of peaks.

Beneficial use of peak formation is studied in a novel approach<sup>78</sup> to electrospinning of polymer nanofibers. A two-layered system is employed with the lower layer being a ferromagnetic suspension and the upper layer a polymer solution. Vertical peaks perturb the interfaces so that when, in addition, an electrical voltage is applied, the perturbations of the free surface are drawn out as in ordinary electrospinning. As the desired result, the production rate of fiber is higher.

**D. Phase Transitions in Ferrofluids.** A phase transition of the gas–liquid type has been observed by a number of investigators in sterically stabilized ferrofluid.<sup>79–81</sup> Upon applying an external magnetic field of critical intensity to a thin layer of the ferrofluid, highly elongated droplets of a concentrated phase of ferromagnetic colloid are formed, having a clearly formed interface separating the drops from a surrounding dilute ferrofluid phase; see Figure 19. When the applied field is removed, the elongated drops are unstable under interfacial tension and break up into smaller spherical drops that diffuse into the surroundings. Instability can also be initiated by adding a less compatible solvent to the ferrofluid. Ionically stabilized ferrofluids undergo phase separation when electrolyte concentration is altered.<sup>83</sup>

This modulational behavior differs in character from our other examples as magnetic particles transfer from one phase to the other, thus changing the concentration in these regions. The phenomenon is rich with magnetochemical content, but a full discussion is outside the scope of this overview.

**E. Modulation of Embedded Objects.** Modulation of embedded objects in a ferrofluid has multiple interests: as a model for two-dimensional melting of solids, for producing periodic structures of large molecules for analysis by scattering

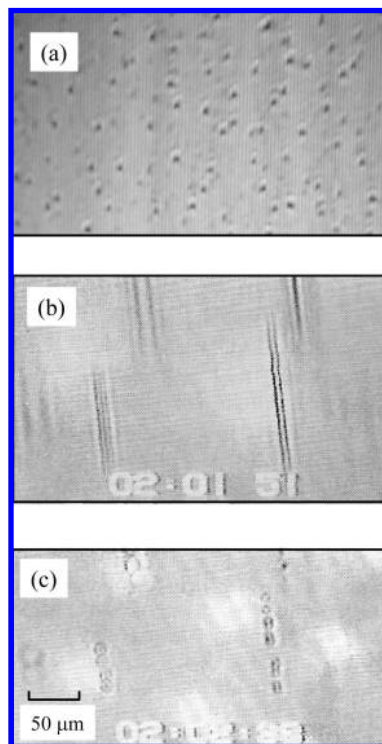


**Figure 19.** (a) Droplets in a thin layer with field oriented normal to the layer of a kerosene-based sterically stabilized ferrofluid. (b) Elongated droplets induced by a  $12.7 \text{ kA m}^{-1}$  magnetic field oriented tangential to the layer. (c) Breakup into spherical droplets  $\sim 0.8 \text{ s}$  after removal of the field permits estimation of interfacial tension,  $\sim 8.1 \times 10^{-4} \text{ mN m}^{-1}$ , based on viscous dominated instability;<sup>82</sup> the droplets subsequently diffuse into the surrounding continuous phase. Parts (b) and (c) are adapted from ref 81. Part (a), not previously published, is taken from a video recording.

of waves, for self-organized manufacturing of microscopic arrays, and so forth.

To a first approximation, when a spherical nonmagnetic particle is dispersed in a magnetized ferrofluid, the void produced by the particle possesses an effective magnetic moment,  $m$ , equal in size but opposite in direction to the magnetic moment of the displaced fluid, that is,  $m = -\mu_0 V \chi H$ , where  $V$  is volume of the sphere,  $\chi$  is the effective volume susceptibility of the ferrofluid, and  $H$  is the magnetic field. For relatively low fields ( $\mu_0 H < 0.01 \text{ T}$ ),  $\chi$  is approximately constant, and  $m$  increases linearly with  $H$ . The interaction energy between two spheres with a center-to-center separation distance of  $r_d$  is given by the dipolar relationship

$$U = \frac{m^2(1 - 3 \cos^2 \theta)}{4\pi\mu_0 r_d^3} \quad (20)$$

$\theta$  is the angle between the line connecting the centers of the spheres and the direction of the field. A thermodynamic system is obtained by using sufficiently small spheres (of diameter  $d < 2 \text{ }\mu\text{m}$ ) having Brownian motion. The controlling parameter determining structural modulation is the ratio between the dipolar energy and the thermal energy. From eq 20, using the magnitude of  $U$  with  $\theta = 0$ ,  $r_d = d$ , and ignoring a constant factor



$$\frac{\text{Dipolar energy}}{\text{Thermal energy}} = \frac{m^2/\mu_0 d^3}{k_B T} \quad (21)$$

A monolayer of equal size nonmagnetic spheres immersed in a thin layer of magnetic fluid yields an intriguing model exhibiting phase change properties of melting.<sup>84</sup> This analogue model utilizes micrometer-size polystyrene spheres that exhibit Brownian motion and can be viewed under a microscope as depicted in Figure 20a. Figure 20b shows that crystalline ordering of the spheres results from the application of a magnetic field oriented perpendicular to the layer. Each sphere is a hole in the magnetic fluid and acts as a magnetic dipole of reverse polarity repelled from its neighbors. Varying the field in this system changes the value of  $m$  and, hence, that of the ratio in eq 21 and can be considered as an adjustment of temperature in a molecular system. Thus, for example, melting or return to randomness is observed if the field is reduced. The system has been suggested for testing theories of two-dimensional melting via the vortex unbinding mechanism.<sup>15</sup> Shown in Figure 20c is the chain formation that results from a tangential orientation of the field. In this configuration, the spheres attract each other.

Ordering of dilute suspensions of macromolecules is attainable in magnetized ferrofluids for assemblies that are not amenable to conventional alignment techniques. Using this technique to obtain neutron diffraction patterns permits study of the internal structure of macromolecules such as the tobacco mosaic virus (TMV) and tobacco rattle virus (TRV).<sup>85</sup> TMV is a hollow cylindrical assembly of length 300 nm, external diameter 18 nm, and internal diameter 4 nm. Similarly, TRV is 23 nm in diameter, 5 nm in internal diameter, and shorter than TRV. TMV and TRV both align when dispersed in a ferrofluid and subjected to a modest level of magnetic field. The ability of the method to work with low concentrations makes the method of particular interest for aligning biological materials such as chromatin, which are not easily obtainable in quantity.

## VII. Patterning Overview

The patterns discussed in this paper have in common that they are generated as the result of a competition between disparate physical influences. Here, we briefly categorize the influences responsible for the modulations in the various cases. Although other interesting patterns exist in dynamical systems, we restrict ourselves to systems in thermodynamic equilibrium where the state (and hence the specific pattern) is determined by free-energy minimization.

The physical influences are energetics of charge exchange, magnetic or electric dipolar interaction, interfacial energy, geometric constraint, and entropic effects, see Figure 21. Patterning in garnet films results from a competition between short-range energetics due to charge exchange (of quantum mechanical origin) and long-range dipolar interaction with the resultant scale of patterning in the micron range. The combination of interfacial energy, which is short-range and of chemical origin, with dipolar long-range energetics gives rise to the patterning of Langmuir monolayers having scale in the micron range and the patterns in the millimeter range of the ferrofluid and dielectric fluids labyrinths, as well as the centimeter scale patterning in the normal-field instability. Block copolymer patterning arises from the interaction of interfacial and entropic influences with a length scale in the submicron range, while in ferrofluids, entropic and dipolar influences interact to produce phase change with a structure in the micron range. Finally, in the case of the ferrofluid composites, the lateral scale of the

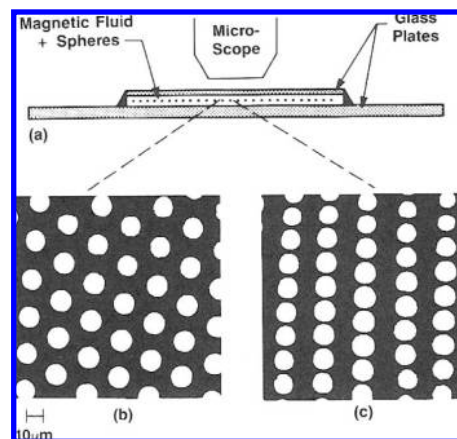


**Figure 20.** (a) A side view of a single layer of nonmagnetic, micrometer-size spheres immersed in ferrofluid. (b) The layer organizes into a hexagonal lattice when the field is oriented normal to the layer and (c) into chains when the field is tangential to the layer. A uniform volumetric magnetization is equivalent to a distribution of poles on the surface of the spheres. These poles confer strong diamagnetic character to the spheres. Adapted from ref 84.

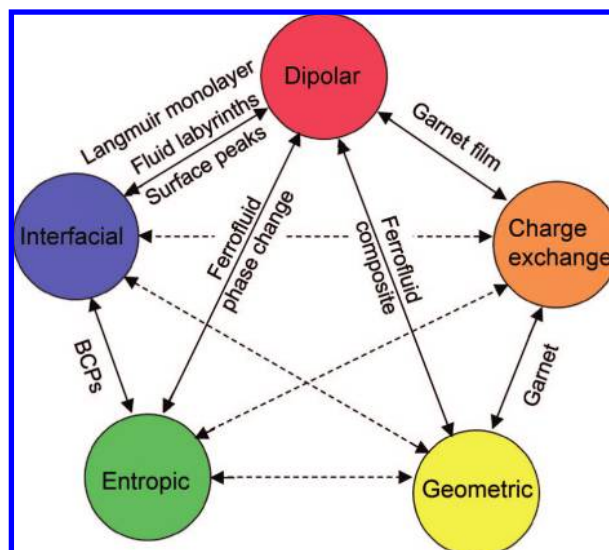


**Figure 21.** A classification of modulated equilibrium systems. Circled parameters represent physical influences. Solid bonds indicate couplings and the resultant patterns. Dashed bonds indicate possibly undiscovered couplings.

chains, typically in the micron range, is determined by the size of the nonmagnetic particles of the mixture under the influence of dipolar energetics.

The various systems with their competing interactions are schematically illustrated in Figure 21. Again the particular coupling of interactions determines the characteristic length scale of the resultant patterns which range in size from the atomic to beyond the millimeter in scale. The patterning in most of these systems is essentially two-dimensional, and this is largely due to a geometrical setup that imposes a spatial constraint. As there are only a limited number of simple geometric patterns, it is not surprising that similar ones are generated at the different length scales. In block copolymer systems, more complex three-dimensional ordered patterns (such as gyroid and cubic phases) have been observed and analyzed, as was seen in Figure 5.

Hierarchical behavior arises in these systems. As an example, the magnetic particles of a ferrofluid are small enough that each of them represents a single ferromagnetic domain, as determined

by charge exchange in competition with a magnetic dipolar influence. However, the patterning of the entire ferrofluid is independent of the micromagnetics of the particles. Instead, it results from the superparamagnetic behavior arising from the collective behavior of an enormous number of the permanently magnetized particles.

### VIII. Concluding Remarks

We considered modulated phases in a broad context encompassing scales ranging from the nano- to the macroscale in diverse solid-state and liquid materials. In equilibrated systems, the structure that develops is often due to a competition between the various energies associated with the structure and yields interesting visual patterning. We concentrated on systems where an external electric field or magnetic one has a strong effect on the system structure, its interfacial properties, and instabilities. Such well-controlled external fields (together with temperature) can facilitate fabrication and control of the desired structure and attributes even on a length scale as small as the nanoscopic one and offer many challenges for future research and applications.

**Acknowledgment.** This paper is dedicated to the memory of Pierre-Gilles de Gennes, a great scientist and close friend, who, with his characteristic gleefulness and insight, stimulated and supported us in our own studies, and he greatly contributed to areas of the modulated systems we reviewed. We thank M. Schick for valuable comments and suggestions. D.A. acknowledges support from the Israel Science Foundation (ISF) under Grant No. 231/08 and the U.S.–Israel Binational Foundation (BSF) under Grant No. 2006055.

### References and Notes

- (1) Seul, M.; Andelman, D. *Science* **1995**, *267*, 476–483.
- (2) (a) Seul, M.; Monar, L. M.; O’Gorman, L. *Philos. Mag. B* **1992**, *66*, 471. (b) Seul, M.; Wolfe, R. *Science* **1991**, *254*, 1616.
- (3) (a) Rosensweig, R. E. *Ferrohydrodynamics*; Cambridge University: New York, 1985. Reprinted with minor updates by Dover: Mineola, NY, 1997. (b) See also: Blums, E.; Cebers, A.; Maiorov, M. M. *Magnetic Fluids* W. de Gruyter, New York, 1997. (c) Andelman, D.; Rosensweig, R. E. *The Phenomenology of Modulated Phases: From Magnetic Solids and Fluids to Organic Films and Polymers*. To be published in: *Polymers, Liquids and Colloids in Electric Fields: Interfacial Instabilities, Orientation and Phase-Transitions*, Tsori Y.; Steiner, U., Eds., World Scientific: Singapore, 2009.
- (4) Rosensweig, R. E.; Zahn, M.; Shumovich, R. J. *Magn. Magn. Mater.* **1983**, *39*, 127–132.
- (5) Elias, F.; Flament, C.; Bacri, J.-C.; Neveu, S. J. *Phys. I (France)* **1997**, *7*, 711–728.
- (6) (a) Kooy, C.; Enz, U. *Philips Res. Rep.* **1960**, *15*, 7. (b) Cape, J. A.; Lehman, G. W. *J. Appl. Phys.* **1971**, *42*, 5732.
- (7) (a) O’Dell, T. H. *Rep. Prog. Phys.* **1983**, *49*, 509. (b) Eschenfelder, A. H. *Magnetic Bubble Technology*; Springer-Verlag: Berlin, Germany, 1980.
- (8) Dennis, C. L.; Borges, R. P.; Buda, L. D.; Ebels, U.; Gregg, J. F.; Hehn, M.; Jouguet, E.; Ounadjela, K.; Petej, I.; Prejbeanu, I. L.; Thornton, M. J. *J. Phys.: Condens. Matter* **2002**, *14*, R1175–R1262.
- (9) Keller, D. J.; McConnell, H. M.; Moy, V. T. *J. Phys. Chem.* **1986**, *90*, 2311.
- (10) Andelman, D.; Brochard, F.; Joanny, J. F. *J. Chem. Phys.* **1987**, *86*, 3673–3681.
- (11) (a) Huebener, R. P. *Magnetic Flux Structures in Superconductors*; Springer-Verlag: Berlin, Germany, 1979. (b) Faber, T. E. *Proc. R. Soc. London, Ser. A* **1958**, *248*, 460.
- (12) Thomas, E. L.; Witten, T. *Physics Today* **1990**, *21*, 27.
- (13) Hamley, I. W. *The Physics of Block Copolymers*; Oxford University: Oxford, U.K., 1998.
- (14) Tsori, Y.; Andelman, D. *J. Polym. Sci., Part B: Polym. Phys.* **2006**, *44*, 2725–2739.
- (15) Chaikin, P. M.; Lubensky, T. C. *Principle of Condensed Matter Physics*; Cambridge University: New York, 2000.
- (16) Very close to  $T_c$ , it was shown that critical fluctuations can change the nature of the transition; see: Brazovskii, S. A. *Sov. Phys. JETP* **1975**, *41*, 85.
- (17) Garel, T.; Doniach, S. *Phys. Rev. B* **1982**, *226*, 325.
- (18) Hubert, A.; Schäfer, R. *Magnetic Domains — The Analysis of Magnetic Microstructures*; Springer: Berlin, Germany, 1998.
- (19) Gaines, G. L. *Insoluble Monolayers at Lipid-Gas Interfaces*; Wiley Interscience: New York, 1966.
- (20) McConnell, H. M. *Annu. Rev. Phys. Chem.* **1991**, *42*, 171–195.
- (21) Möhwald, M. *Structure and Dynamics of Membranes*; Elsevier: Amsterdam, The Netherlands, 1995.
- (22) Schneider, M. F.; Andelman, D.; Tanaka, M. *J. Chem. Phys.* **2005**, *122*, 094717.
- (23) Bates, F. S.; Fredrickson, G. H. *Physics Today* **1999**, *52*, 32.
- (24) Fredrickson, G. H. *The Equilibrium Theory of Inhomogeneous Polymers*; Oxford University: Oxford, U.K., 2005.
- (25) Park, C.; Yoon, J.; Thomas, E. L. *Polymer* **2003**, *44*, 6725.
- (26) Bucknall, D. G. *Prog. Mater. Sci.* **2004**, *49*, 713.
- (27) Vlasov, Y. A.; Bo, X. Z.; Sturm, J. C.; Norris, D. J. *Nature* **2001**, *414*, 289.
- (28) Fink, Y.; Winn, J. N.; Fan, S.; Chen, C.; Michel, J.; Joannopoulos, J. D.; Thomas, E. L. *Science* **1998**, *282*, 1679.
- (29) Khandpur, A. K.; Foerster, S.; Bates, F. S.; Hamley, I. W.; Ryan, A. J.; Bras, W.; Almdal, K.; Mortensen, K. *Macromolecules* **1995**, *28*, 8796.
- (30) Leibler, L. *Macromolecules* **1980**, *13*, 1602.
- (31) Binder, K.; Frisch, H. L.; Stepanow, S. J. *Phys. II (France)* **1997**, *7*, 1353.
- (32) Fredrickson, G. H.; Helfand, E. J. *Chem. Phys.* **1987**, *87*, 697.
- (33) Ohta, T.; Kawasaki, K. *Macromolecules* **1986**, *19*, 2621.
- (34) Shull, K. R. *Macromolecules* **1992**, *25*, 2122.
- (35) Matsen, M. W.; Schick, M. *Phys. Rev. Lett.* **1994**, *72*, 2660.
- (36) Binder, K. *Acta Polym.* **1995**, *46*, 204.
- (37) Szeleifer, I. *Curr. Opin. Colloid Sci.* **1996**, *1*, 416.
- (38) Tsori, Y.; Andelman, D. *Macromolecules* **2002**, *35*, 5161–5170.
- (39) (a) Amundson, K.; Helfand, E.; Quan, X.; Smith, S. D. *Macromolecules* **1993**, *26*, 2698. (b) Amundson, K.; Helfand, E.; Quan, X.; Hudson, S. D.; Smith, S. D. *Macromolecules* **1994**, *27*, 6559.
- (40) Onuki, A.; Fukuda, J. *Macromolecules* **1995**, *28*, 8788.
- (41) Pereira, G. G.; Williams, D. R. M. *Macromolecules* **1999**, *32*, 8115.
- (42) Thurn-Albrecht, T.; DeRouchey, J.; Russell, T. P. *Macromolecules* **2000**, *33*, 3250.
- (43) Kyrylyuk, A. V.; Zvelindovsky, A. V.; Sevink, G. J. A.; Fraaije, J. G. E. M. *Macromolecules* **2002**, *35*, 1473.
- (44) (a) Böker, A.; Knoll, A.; Elbs, H.; Abetz, V.; Müller, A. H. E.; Krausch, G. *Macromolecules* **2002**, *35*, 1319. (b) Böker, A.; Schmidt, K.; Knoll, A.; Zettl, H.; Hansel, H.; Urban, V.; Abetz, V.; Krausch, G. *Polymer* **2006**, *47*, 849.
- (45) Xu, T.; Zhu, Y.; Gido, S. P.; Russell, T. P. *Macromolecules* **2004**, *37*, 2625–2629.
- (46) Olszowka, V.; Hund, M.; Kuntermann, V.; Scherdel, S.; Tsarkova, L.; Böker, A.; Krausch, G. *Soft Matter* **2006**, *2*, 1089–1094.
- (47) Schmidt, K.; Schoberth, H. G.; Ruppel, M.; Zettl, H.; Hänsel, H.; Weiss, T. M.; Urban, V.; Krausch, G.; Böker, A. *Nat. Mater.* **2008**, *7*, 142–145.
- (48) Matsen, M. W. *Macromolecules* **2006**, *39*, 5512.
- (49) Lin, C.-Y.; Schick, M. *J. Chem. Phys.* **2006**, *125*, 034902.
- (50) (a) Xu, T.; Zvelindovsky, A. V.; Sevink, G. J. A.; Gang, O.; Ocko, B.; Zhu, Y.; Gido, S. P.; Russell, T. P. *Macromolecules* **2004**, *37*, 6980–6984. (b) Xu, T.; Hawker, C. J.; Russell, T. P. *Macromolecules* **2005**, *38*, 2802.
- (51) Tsori, Y.; Tournilhac, F.; Andelman, D.; Leibler, L. *Phys. Rev. Lett.* **2003**, *90*, 145504.
- (52) Tsori, Y.; Andelman, D.; Lin, C.-Y.; Schick, M. *Macromolecules* **2006**, *39*, 289.
- (53) Lin, C.-Y.; Schick, M.; Andelman, D. *Macromolecules* **2005**, *38*, 5766.
- (54) Wang, J.-Y.; Xu, T.; Leiston-Belanger, J. M.; Gupta, S.; Russell, T. P. *Phys. Rev. Lett.* **2006**, *96*, 128301/1–128301/4.
- (55) Massart, R. *IEEE Trans. Magn.* **1981**, *MAG-17* (2), 1247–1248.
- (56) de Gennes, P. G.; Pincus, P. A. *Phys. Kondens. Mater.* **1970**, *11*, 189.
- (57) Rabinow, J. *AIEE Trans.* **1948**, *67*, 1308–1315.
- (58) (a) Weissler, P. Cadillac Magnetic-Rheological Shocks. *Popular Mechanics* **2000**. (b) Jolly, M. R.; Bender, J. W.; Carlson, J. D. *Properties and Applications of Commercial Magnetorheological Fluids Brochure*; Lord Corporation: Cary, NC.
- (59) (a) Kordonsky, W. I., et al. *Magnetorheological Polishing Devices and Methods*. U.S. Patent 6,503,414, 2003; see also: (b) Umehara, N.; Kato, K. *J. Magn. Magn. Mater.* **1987**, *65*, 397–400.
- (60) Rhodes, S.; Perez, J.; Elborai, S.; Lee, S.-H.; Zahn, M. *J. Magn. Magn. Mater.* **2005**, *289*, 353–355.

- (61) Rosensweig, R. E.; Browaeys, J.; Bacri, J.-C.; Zebib, A.; Perzinski, R. *Phys. Rev. Lett.* **1999**, *83*, 4904–4907.
- (62) Richter, R.; Blasing, J. *Rev. Sci. Instrum.* **2001**, *72*, 1729–1733.
- (63) Rosensweig, R. E. *Sci. Am.* **1982**, *247*, 136–145.
- (64) Cowley, M. D.; Rosensweig, R. E. *J. Fluid Mech.* **1967**, *30*, 671–688.
- (65) Essmann, U.; Trauble, H. *Phys. Lett. A* **1967**, *24*, 526–527.
- (66) (a) Gailitis, A. *Magnetohydrodynamics* **1969**, *5*, 44–45. (b) Gailitis, A. *J. Fluid Mech.* **1977**, *82*, 401–413.
- (67) Boudouvis, A. G.; Puchalla, J. L.; Scriven, L. E.; Rosensweig, R. E. *J. Magn. Magn. Mater.* **1987**, *65*, 307–310.
- (68) Abou, B.; Wesfreid, J. E.; Roux, J. *J. Fluid Mech.* **2000**, *416*, 217–237.
- (69) Richter, R.; Barashenkov, I. V. *Phys. Rev. Lett.* **2005**, *94*, 184503/1–184503/4.
- (70) Petrelis, F.; Falcon, E.; Fauve, S. *Eur. Phys. J. B* **2000**, *15*, 3–6.
- (71) Boudouvis, A. G. 2007, private communication.
- (72) Tsebers, A. O.; Maiorov, M. M. *Magnetohydrodynamics* **1980**, *16*, 21–28.
- (73) Jackson, D. P.; Goldstein, R. E.; Cebers, A. O. *Phys. Rev. E* **1994**, *50*, 298–307.
- (74) Cebers, A. O. *Braz. J. Phys* **2001**, *31*, 441–445.
- (75) Rosensweig, R. E. 1982, unpublished photographs.
- (76) Elias, F.; Flament, C.; Bacri, J.-C.; Cardoso, O.; Graner, F. *Phys. Rev. E* **1997**, *56*, 3310–3318.
- (77) Borra, E. F.; Ritcey, A. M.; Bergamasco, R.; Laird, P.; Gringras, J.; Dallaire, M.; Da Silva, L.; Yockell-Lelievre, H. *Astron. Astrophys.* **2004**, *419*, 777–782.
- (78) Yarin, A. L.; Zussman, E. *Polymer* **2004**, *45*, 2977–2980.
- (79) Hayes, C. F. *J. Colloid Interface Sci.* **1975**, *52*, 239–243.
- (80) Baryakhtar, F. G.; Gorobets, Yu I.; Kosachevskii, Ya.; Il'chishin, O. V.; Khizhenkov, P. K. *Magn. Gidrodin.* **1981**, *3*, 120–123.
- (81) Rosensweig, R. E.; Popplewell, J. Electromagnetic Forces and Applications. *Int. J. Appl. Electromag. Mater.* **1992**, *2*, 83–86.
- (82) Stone, H. A.; Brenner, M. P. *J. Fluid Mech.* **1996**, *318*, 373–374. The relaxation time in the viscous mode of instability is orders of magnitude slower than that for inviscid breakup and hence dominates. Accordingly, this estimate of interfacial tension corrects the value estimated in ref 81.
- (83) Bacri, J.-C.; Perzynski, R.; Salin, D.; Cabuil, V.; Massart, R. *J. Colloid Interface Sci.* **1989**, *132*, 43–53.
- (84) (a) Skjeltorp, A. T. *Phys. Rev. Lett.* **1983**, *51*, 2306–2309. (b) Skjeltorp, A. T. *J. Appl. Phys.* **1985**, *57*, 3285–3290.
- (85) Hayter, J. B.; Pynn, R.; Charles, S.; Skjeltorp, A. T.; Trehwella, J.; Stubbs, G.; Timmins, P. *Phys. Rev. Lett.* **1989**, *62*, 1667–1672.

JP807770N